An archaeal compound as a driver of Parkinson's disease pathogenesis

Paul Wilmes (paul.wilmes@uni.lu)
University of Luxembourg https://orcid.org/0000-0002-6478-2924

Jean-Pierre Trezzi
University of Luxembourg

Velma Aho
University of Luxembourg https://orcid.org/0000-0003-2916-7018

Christian Jäger
University of Luxembourg https://orcid.org/0000-0003-4235-7430

Sebastian Schade
Paracelsus-Elena-Klinik Kassel https://orcid.org/0000-0002-6316-6804

Annette Janzen
Philipps-University Marburg

Oskar Hickl
University of Luxembourg

Benoit Kunath
University of Luxembourg

Mélanie Thomas
University of Luxembourg

Kristopher Schmit
University of Luxembourg

Pierre Garcia
University of Luxembourg

Alessia Sciortino
University of Luxembourg

Camille Martin-Gallausiaux
University of Luxembourg

Rashi Halder
Luxembourg Centre for Systems Biomedicine, University of Luxembourg https://orcid.org/0000-0002-1402-1254

Oihane Uriarte Huarte
University of Luxembourg

Tony Heurtaux
University of Luxembourg

Ursula Heins-Marroquin
University of Luxembourg
Gemma Gomez-Giro
University of Luxembourg
Katrin Weidenbach
Christian-Albrechts-Universität zu Kiel
Léa Delacour
University of Luxembourg
Cédric Laczny
University of Luxembourg
Polina Novikova
University of Luxembourg
Javier Ramiro-Garcia
Spanish National Research Council https://orcid.org/0000-0003-3896-3833
Randolph Singh
University of Luxembourg
Begoña Talavera Andújar
University of Luxembourg
Laura Lebrun
Luxembourg Centre for Systems Biomedicine, University of Luxembourg
Annegrait Daujeumont
University of Luxembourg
Janine Habier
University of Luxembourg
Xiangyi Dong
University of Luxembourg
Floriane Gavotto
University of Luxembourg
Anna Heintz-Buschart
SILS https://orcid.org/0000-0002-9780-1933
Jochen Schneider
University of Luxembourg
Nico Jehmlich
Helmholtz-Centre for Environmental Research - UFZ https://orcid.org/0000-0002-5638-6868
Martin von Bergen
UFZ-Helmholtz-Centre for Environmental Research https://orcid.org/0000-0003-2732-2977
Emma Schymanski
University of Luxembourg https://orcid.org/0000-0001-6868-8145
Ruth Schmitz

Christian-Albrechts-University Kiel https://orcid.org/0000-0002-6788-0829
Jens Schwamborn
University of Luxembourg https://orcid.org/0000-0003-4496-0559
Enrico Glaab
Université du Luxembourg, Luxembourg Centre for Systems Biomedicine https://orcid.org/0000-0003-3977-7469
Carole Linster
University of Luxembourg https://orcid.org/0000-0001-7143-0719
Toshimori Kitami
RIKEN Center for Integrative Medical Sciences
Manuel Buttini
University of Luxembourg
Patrick May
University of Luxembourg https://orcid.org/0000-0001-8698-3770
Claudia Trenkwalder
Paracelsus-Elena-Klinik Kassel
Wolfgang Oertel
Brit Mollenhauer
University Medical Center Göttingen

Biological Sciences - Article

Keywords:

Posted Date: July 26th, 2022

DOI: https://doi.org/10.21203/rs.3.rs-1827631/v1

An archaeal compound as a driver of Parkinson's disease pathogenesis

Jean-Pierre Trezzi[1,2§], Velma T. E. Aho[1§], Christian Jäger[1], Sebastian Schade[3,4], Annette Janzen[5], Oskar Hickl[1], Benoit Kunath[1], Mélanie H. Thomas[1,6], Kristopher J. Schmit[1,6], Pierre Garcia[1,6], Alessia Sciortino[1,6], Camille Martin-Gallausiaux[1], Rashi Halder[1], Oihane Uriarte Huarte[1,6], Tony Heurtaux[6,7], Ursula Heins-Marroquin[1], Gemma Gomez-Giro[1], Katrin Weidenbach[8], Léa Delacour[1], Cédric C. Laczny[1], Polina V. Novikova[1], Javier Ramiro-Garcia[1], Randolph R. Singh[1,9], Begoña Talavera Andújar[1], Laura A. Lebrun[1], Annegrait Daujeumont[1], Janine Habier[1], Xiangyi Dong[1], Floriane Gavotto[1], Anna Heintz-Buschart[10], NCER-PD Consortium, Jochen G. Schneider[1,11], Nico Jehmlich[12], Martin von Bergen[12], Emma L. Schymanski[1], Ruth A. Schmitz[8], Jens C. Schwamborn[1], Enrico Glaab[1], Carole L. Linster[1], Toshimori Kitami[13], Manuel Buttini[1,6], Patrick May[1], Claudia Trenkwalder[4,14], Wolfgang Oertel[5], Brit Mollenhauer[3,4], Paul Wilmes[1,7*]

1. Luxembourg Centre for Systems Biomedicine, University of Luxembourg, Esch-sur-Alzette, Luxembourg
2. Integrated Biobank of Luxembourg, Luxembourg Institute of Health, Dudelange, Luxembourg
3. Department of Neurology, University Medical Center Göttingen, Göttingen, Germany
4. Paracelsus-Elena-Klinik, Kassel, Germany
5. Department of Neurology, Philipps-University Marburg, Marburg, Germany
6. Luxembourg Center of Neuropathology (LCNP), Dudelange, Luxembourg

22 7. Department of Life Sciences and Medicine, Faculty of Science, Technology and Medicine,
23 University of Luxembourg, Belvaux, Luxembourg
24 8. Institute for General Microbiology, Christian-Albrechts-Universität zu Kiel, Kiel, Germany
25 9. Unité Contamination Chimique des Ecosystèmes Marins, IFREMER (Institut Français de
26 Recherche pour l'Exploitation de la Mer), Nantes, France
27 10. Biosystems Data Analysis, Swammerdam Institute for Life Sciences, Faculty of Science,
28 University of Amsterdam, Amsterdam, The Netherlands
29 11. Departments of Internal Medicine and Psychiatry and Psychotherapy, Saarland University
30 Medical Center at Homburg/Saar, Homburg, Germany
31 12. Helmholtz-Zentrum für Umweltforschung – UFZ GmbH, Department Molekulare
32 Systembiologie, Leipzig, Germany
33 13. RIKEN Center for Integrative Medical Sciences, Kanagawa, Japan
34 14. Department of Neurosurgery, University Medical Center Göttingen, Göttingen, Germany
35
36 § These authors contributed equally to this work
37 * Corresponding author: Paul Wilmes, paul.wilmes@uni.lu, (+352) 46 66 44 6188
38
39

Abstract

Patients with Parkinson's disease (PD) exhibit differences in their gut microbiomes compared to healthy individuals[1–3]. Although differences have most commonly been described in the abundances of bacterial taxa, changes to viral and archaeal populations have also been observed[3–5]. Mechanistic links between gut microbes and PD pathogenesis remain elusive but could involve molecules that promote α-synuclein aggregation[1,6]. Here, we show that 2-hydroxypyridine (2-HP) represents a key molecule for the pathogenesis of PD. We observe significantly elevated 2-HP levels in faecal samples from patients with PD or its prodrome, idiopathic REM sleep behaviour disorder (iRBD), compared to healthy controls. 2-HP is correlated with the archaeal species *Methanobrevibacter smithii* and with genes involved in methane metabolism, and it is detectable in isolate cultures of *M. smithii*. We demonstrate that 2-HP is selectively toxic to transgenic α-synuclein overexpressing yeast and increases α-synuclein aggregation in a yeast model as well as in human induced pluripotent stem cell derived enteric neurons. It also exacerbates PD-related motor symptoms, α-synuclein aggregation, and striatal degeneration when injected intrastriatally in transgenic mice overexpressing human α-synuclein. Our results highlight the effect of an archaeal molecule in relation to the gut-brain axis, which is critical for the diagnosis, prognosis, and treatment of PD.

Main

Changes to the gut microbiome have been implicated in the pathogenesis of idiopathic conditions such as cancer, autoimmune, metabolic, and neurodegenerative diseases. For all, incidences have been rising in the past decades[7–11]. However, the causal mechanisms remain largely elusive, not least for disorders such as Parkinson's disease (PD), where connections between distal body sites (the gut) and organs classically associated with the disease (the brain) are not obvious. Nevertheless, as the hub of exposures to microbiome-derived molecules, the gut represents a main candidate site for the initiation of pathogenic processes which may subsequently spread systemically, for example via the gut-brain axis[6,12].

Cross-sectional studies have highlighted microbial community differences in the gut of PD patients compared to healthy control subjects[1,3,6]. Changes in microbial abundances have also been identified in patients with idiopathic rapid eye movement sleep behaviour disorder (iRBD)[13], which is recognized as a prodromal stage of α-synucleinopathies[14]. A smaller number of studies have explored specific molecules, such as faecal short-chain fatty acids (SCFAs)[15,16], or used multi-omic and computational approaches to identify microbial genes or functions which may be enriched or depleted in PD[4,5,17]. However, although agreement exists in relation to taxa found to be enriched in PD including the genera *Akkermansia*, *Bifidobacterium* and *Lactobacillus*[2,3], there is currently no consensus on the functional impact of these microbes on PD pathogenesis, or even whether their role is causal or not.

Multi-omic approaches that provide detailed information on the functional attributes of the microbiome are essential for understanding the molecular links between microbes and disease[18].

83 Here, we performed an integrated multi-omic analysis of faecal samples from PD and iRBD
84 patients and healthy control subjects to systematically investigate the functional consequences of
85 altered gut microbiota in PD. Untargeted metabolomics results revealed an initially unidentified
86 candidate molecule, which was significantly enriched in PD and iRBD and which we identified as
87 2-hydroxypyridine (2-HP; tautomer: 2-pyridone). We characterized the effects of this molecule in
88 cellular and animal models of PD pathogenesis, which uncovered an effect on relevant α-synuclein
89 aggregation, and an association with hydrogenotrophic methanogenic archaea which were
90 identified as the likely source.
91

92 **Integrated multi-omic analyses**

93 Our initial set of subjects consisted of 50 PD and 30 iRBD cases as well as 50 control subjects; 4
94 PD and 3 iRBD cases as well as 1 control subject were subsequently excluded due to reasons
95 described in the Supplementary Methods. Using our previously developed methodological
96 framework[19,20], we performed a systematic multi-omic analysis of DNA, RNA, proteins, and
97 metabolite fractions isolated from flash-frozen faecal samples obtained from 46 PD and 27 iRBD
98 patients as well as 49 healthy controls (Extended Data Fig 1, Extended Data Table 1a). Statistical
99 comparisons were performed for seven data types: taxonomically and functionally annotated
100 metagenomic (MG), metatranscriptomic (MT) and metaproteomic (MP) data, as well as metabolite
101 data (Extended Data Fig 2, Supplementary Tables 1-3, Supplementary Discussion). Taxonomic
102 comparisons revealed no differences in alpha diversity with any data type or metric, while beta
103 diversity differed significantly between cases (subjects with either PD or iRBD) and controls in
104 MT and MG data when adjusted for age and sex (Extended Data Fig 3a-b, Supplementary Table
105 4). Many previously reported differences between specific microbial taxa were replicated,

106 particularly in the MT data (Extended Data Fig 3c-d, Supplementary Tables 5-6). This data type
107 also had the largest number of differentially abundant features in functionally annotated data
108 (Extended Data Fig 3e-f, Supplementary Tables 7-8), emphasising the importance of using
109 multiple omic datasets instead of focusing on DNA-based analyses. Metabolite comparisons
110 highlighted significantly elevated levels of two unidentified compounds in iRBD and PD (Fig 1a-
111 b, Extended Data Fig 4a, Supplementary Table 9). An integrated analysis of all omic datasets
112 (Extended Data Fig 5, Supplementary Table 10) also selected these compounds among the features
113 that best differentiate between cases and controls.

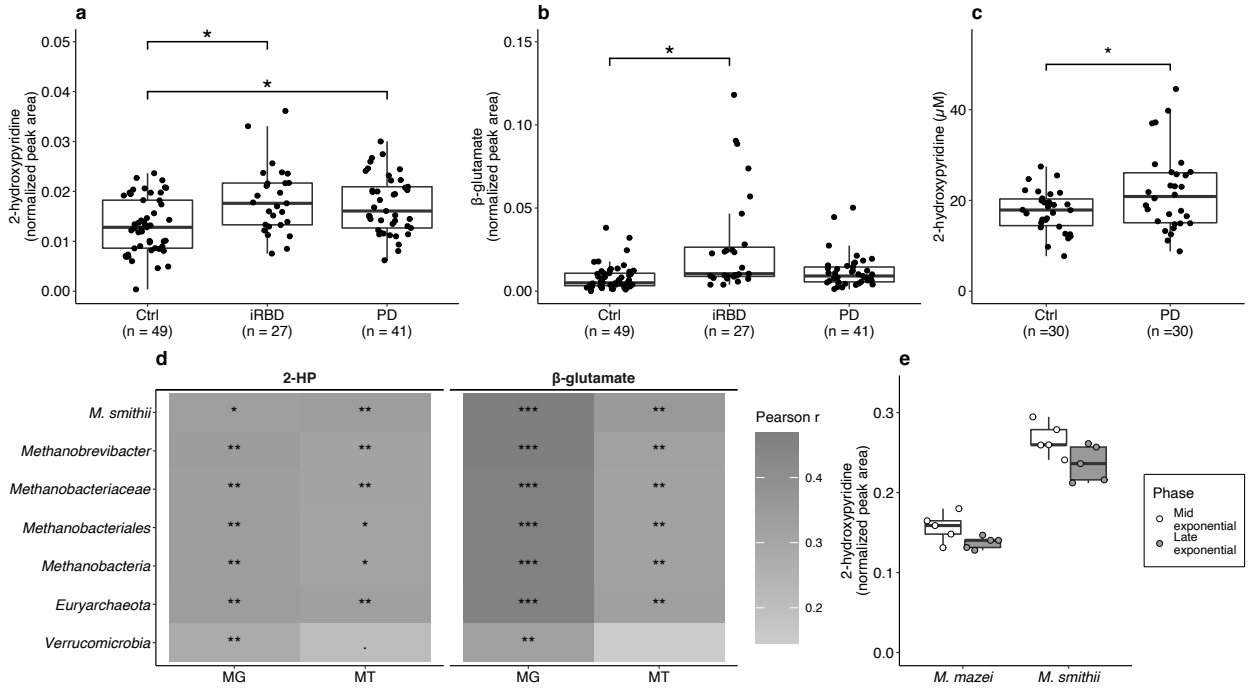

114

115 **Figure 1: Metabolite differences between case and control subjects, and findings connecting**
116 **differentially abundant metabolites to the gut archaeon *Methanobrevibacter smithii*. a.** Normalized
117 peak area of 2-hydroxypyridine (2-HP) in faecal extracts of PD and iRBD patients and control subjects
118 (Ctrl). **b**. Normalized peak area of β-glutamate in faecal extracts from PD and iRBD patients and control
119 subjects. **c.** Validation of differential concentration of 2-HP in faecal extracts with targeted metabolomics.
120 **d.** Pearson correlations of relative abundances of taxa with 2-HP and β-glutamate, trimmed to taxa with the
121 most overlap between different analysis strategies (complete results: Extended Data Fig 4d and
122 Supplementary Table 17); MG = metagenomic data, MT = metatranscriptomic data. **e.** 2-HP in cells of the
123 archaeal species *Methanobrevibacter smithii* (*M. smithii*) and *Methanosarcina mazei* (*M. mazei*); five
124 biological replicates, normalized by cell count prior to measurement. In a-c, *P*-values reflect unpaired, two-

125 tailed t-tests corrected for multiple comparisons across all metabolites; * $P < 0.05$. In all box plots: box
126 hinges: 1st and 3rd quartiles; whiskers: hinge to highest/lowest values that is within 1.5*IQR of hinge.
127

128 The first unidentified metabolite was significantly correlated with disease duration in PD patients
129 (P=0.025 for Pearson correlation; Extended Data Fig 4b, Supplementary Table 11). This
130 metabolite was annotated as 2-hydroxypyridine by matching its electron ionization mass spectrum
131 against publicly available mass spectral libraries (e.g. the Golm Metabolome Database[21]). Finally,
132 a commercially available chemical standard was used for definitive identification by its mass
133 spectral fingerprint and retention index. We further validated the difference in 2-HP between PD
134 patients and controls with targeted metabolomics (Fig 1c) using 60 additional faecal samples (30
135 PD, 30 controls, Extended Data Table 1b).

136

137 2-HP is a microbial degradation product of chlorpyrifos[22], a pesticide known to increase the risk
138 of PD[23]. We explored our faecal LC-MS/MS data for the presence of this pesticide but did not
139 detect it or related molecules (Supplementary Tables 12-16, Supplementary Discussion). In
140 comparisons with other data types (Extended Data Fig 4d-f, Supplementary Tables 17-19,
141 Supplementary Discussion), 2-HP was significantly correlated with the metagenomic (MG) and
142 metatranscriptomic (MT) abundances of archaea, specifically of *Methanobrevibacter smithii*
143 (P=0.006 in MT and P=0.014 in MG relative abundances with false discovery rate (fdr) -adjusted
144 Pearson correlation; Fig 1d, Extended Data Fig 4d, Supplementary Table 17). *M. smithii,* a
145 hydrogenotrophic methanogen, is the most abundant archaeal species in the human gastrointestinal
146 tract[24]. It is associated with constipation[25], which is also a common early non-motor symptom of
147 PD[26]. Although *M. smithii* exhibited a numerically higher mean relative abundance in PD and
148 iRBD subjects in taxon data, the difference to controls was not statistically significant in any omic

149 dataset (Extended Data Fig 6a-c, Supplementary Tables 5-6). This could be due to the overall low
150 levels of archaea in the gut, and the fact that our methodological workflow was not optimised for
151 archaeal detection. However, a significant increase in the genus *Methanobrevibacter* in PD was
152 previously reported in a meta-analysis combining 16S rRNA gene amplicon data from nine
153 studies[3]. Furthermore, we detected a significantly higher abundance of this genus in faecal samples
154 from an independent PD cohort from Luxembourg (NCER-PD cohort[17], 343 controls and 194 PD
155 patients; Extended Data Table 1c, Extended Data Fig 6d, Supplementary Table 20). Finally,
156 considering functionally annotated MG and MT data from the main cohort of the present study, 2-
157 HP was significantly correlated with more than half of the methanogenesis-related gene functions
158 from *M. smithii* detected in data from cases, but not in data from control subjects (Extended Data
159 Fig 6e).
160
161 The second unidentified metabolite, which was particularly elevated in iRBD compared to
162 controls, was identified as β-glutamate. We found it to also be correlated with *M. smithii* relative
163 abundance (fdr-adjusted $P = 0.001$ for Pearson correlation of relative abundance in MT data and
164 $P < 0.001$ in MG data; Extended Data Fig 4d, Supplementary Table 17). β-glutamate is a known
165 archaeal osmolyte[27], thereby further supporting a connection between PD and archaeal
166 metabolism. 2-HP and β-glutamate were also positively correlated (Extended Data Fig 4e,
167 Supplementary Table 18). Other signals that were highly correlated with both 2-HP and β-
168 glutamate were analytes with such low abundances in the samples that structure elucidation based
169 on electron ionization mass spectrum interpretation was not possible.
170

171 We hypothesized that archaeal metabolism could be the main source of the increased 2-HP levels
172 in PD and iRBD patients' faecal samples. One potential source could be the cofactor of the enzyme
173 5,10-methenyltetrahydromethanopterin hydrogenase (Hmd), which is produced by
174 hydrogenotrophic methanogenic archaea, as this cofactor contains a 2-pyridone structure[28]. To
175 confirm the presence of 2-HP in *M. smithii*, we measured it in cultures of the type strain of this
176 species, as well as of an environmental methanogenic archaeal species not found in the gut,
177 *Methanosarcina mazei*. 2-HP was detectable in cells of both species, with higher levels at mid-
178 exponential compared to late-exponential phase (Fig 1e).
179
180 We additionally quantified 2-HP in cerebrospinal fluid (CSF) and plasma samples from a subset
181 of subjects. It was not detectable in CSF but was detectable at low levels in plasma (Extended Data
182 Fig 4c), although concentrations did not differ between cases and controls. This indicates that 2-
183 HP can pass from the gut to circulation and could therefore trigger systemic effects beyond the
184 gut. Three different computational prediction tools[29–31] suggest, at high-confidence, that it can also
185 penetrate the blood-brain-barrier.
186
187 2-HP shares a substructure with the curlicide/pilicide FN075, which contains a ring-fused 2-
188 pyridone[32]. This compound inhibits fibrillation of the amyloidogenic curli protein CsgA, but
189 stimulates α-synuclein amyloid fibre formation[32]. Based on this common substructure, we
190 hypothesized that 2-HP could also influence α-synuclein aggregation, providing a potential
191 mechanistic connection to PD pathogenesis, and prompting us to study the effect of 2-HP on α-
192 synuclein aggregation and neurotoxicity.
193

194 **2-hydroxypyridine and α-synuclein**

195 One of the main histopathological hallmarks of PD is the formation of intracellular inclusions
196 known as Lewy bodies, the main constituent of which is α-synuclein[33]. We used multiple
197 experimental approaches with appropriate concentrations, including an *in vivo* model, to explore
198 the connection between 2-HP and α-synuclein aggregation.

199

200 First, we used a yeast model overexpressing human α-synuclein, HiTox. In agreement with human
201 PD pathology, galactose-inducible expression of α-synuclein in yeast leads to cytosolic α-
202 synuclein aggregation and severe growth defects by disrupting vesicle trafficking, mitochondrial
203 function and lipid homeostasis[34–37]. These phenotypes have been translated in human-derived cell
204 models, demonstrating the strength of this model to study cellular α-synuclein-induced
205 cytotoxicity[37,38]. Based on preliminary testing, micromolar concentrations had no detectable
206 effects, and a range of 1 mM to 100 mM was chosen for the subsequent experiments. We confirmed
207 that at these levels, 2-HP exacerbates α-synuclein-induced toxicity in the HiTox model in a dose-
208 dependent manner (Fig 2a, Extended Data Fig 7a). Growth defects were already seen at 1 mM,
209 and a 100 mM concentration was almost lethal. In contrast, the control strain, which does not
210 express human α-synuclein, showed a slight growth improvement in the presence of higher doses
211 of 2-HP. When α-synuclein expression was not induced, both strains showed only a mild growth
212 defect at 100 mM (Extended Data Fig 7a-b), confirming that 2-HP is toxic only when the strain
213 expresses human α-synuclein. We additionally tested two related compounds, namely 3-
214 hydroxypyridine (3-HP) and 4-hydroxypyridine (4-HP). 4-HP had only a mild effect on the HiTox
215 strain at 30 mM and above, while 3-HP was very toxic to both strains at concentrations above 10
216 mM (Extended Data Fig 7c). Based on this, 2-HP has the clearest dose-response effect when

217 compared to the two other hydroxypyridine isomers. Furthermore, microscopic inspection of the
218 HiTox strain under moderately toxic conditions (30 mM 2-HP) revealed a significant increase in
219 cells with cytosolic α-synuclein aggregates in comparison to the control conditions (Fig 2b-c).
220 Taken together, our results demonstrate that 2-HP stimulates α-synuclein aggregation and
221 exacerbates its cytotoxic effect in the HiTox yeast model.

222

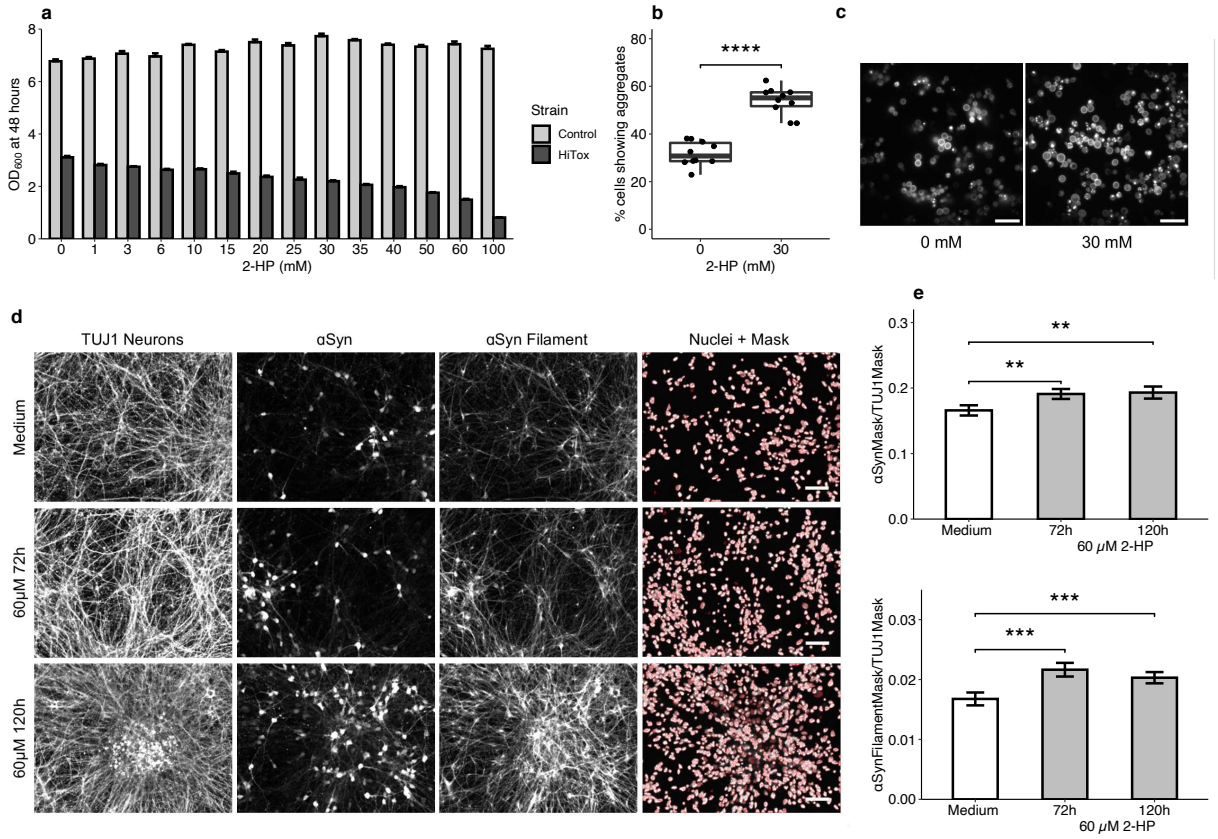

223

224 **Figure 2. Effects of 2-hydroxypyridine in human α-synuclein expressing yeast model and in human**
225 **induced pluripotent stem cell (hiPSC) derived enteric neurons. a.** Dose-response assay in α-synuclein
226 expressing yeast cells (HiTox) and control strain (Ctrl); showing means and standard deviations calculated
227 from four biological replicates for each strain. **b.** Microscopy-based quantification of yeast cells exhibiting
228 α-synuclein aggregates (based on 10 pictures per condition). Box hinges: 1st and 3rd quartiles; whiskers:
229 hinge to highest/lowest values that is within 1.5*IQR of hinge. **c.** Representative microscopy images of
230 HiTox cells after 24 h treatment with 30 mM 2-HP; scale bar: 20 µm. **d**. High-content imaging of hiPSC
231 derived enteric neurons, showing total α-synuclein (αSyn), α-synuclein filament (αSyn Filament), TUJ1-
232 positive neurons and Hoechst-positive nuclei (with a representation of the mask applied to segment the

233 nuclei); scale bar: 100 μm. **e.** Total α-synuclein and filamentous α-synuclein normalized to the amounts of
234 TUJ1-positive neurons (mean ± SEM of three independent neuronal differentiations; 8 wells per condition
235 and 30 fields per well quantified for each). * $P < 0.05$, ** $P < 0.01$, *** $P < 0.001$, **** $P < 0.0001$.

236

237 To further evaluate the toxicity of 2-HP in human induced pluripotent stem cell (iPSC)-derived
238 enteric nervous system (ENS) neurons[39] (Extended Data Fig 8a-b), we treated ENS cells with 60
239 μM 2-HP, the highest concentration that did not severely impair cell viability in preliminary dose
240 tests. After 120 hours of exposure, we did not observe a significant decrease in the viability of the
241 cultures (Extended Data Fig 8c). However, we observed a significant increase in both total and
242 fibrillated α-synuclein (Fig 2d-e) with a concomitant increase in the apoptotic marker cleaved-
243 caspase 3 (CC3) (Extended Data Fig 8d-e), supporting that exposure to 2-HP also drives α-
244 synuclein accumulation in ENS neurons.

245

246 Finally, we explored the effects of 2-HP on the central nervous system (CNS) *in vivo* using an
247 established experimental approach for studying the effect of α-synuclein toxicity-promoting agents
248 in mice[40,41]. We performed intrastriatal injections of 100 mM 2-HP into a mouse model
249 overexpressing human wild-type *SNCA* (hSNCA) under the transcriptional control of the neuronal
250 Thy1 promoter, and wild-type littermate controls. The concentration was selected based on
251 previous literature of neurodegeneration-inducing molecules for which the dose used in stereotaxic
252 injections *in vivo* is typically 100 x higher than the one used *in vitro*[42]. The mice were all
253 heterozygous for the transgene, males, and 2-3 months old. Two months after the injection, we
254 observed that fine motor skills, assessed with the adhesive removal test[43], were significantly
255 impaired in hSNCA mice injected with 2-HP compared to those injected with vehicle solution
256 without 2-HP (Fig 3a). To determine the pathological basis of the impairment, we measured the

relative levels of tyrosine-hydroxylase (TH), a marker for dopaminergic neurons and their projecting fibres into the dorsal striatum[40]. We found that TH was significantly reduced in the dorsal striatum, and somewhat reduced in the substantia nigra pars compacta (SNpc) in the 2-HP injected hSNCA mice (Fig 3b-c). We also measured S129 phosphorylated α-synuclein (phospho-αSyn), the most commonly used marker to identify α-synuclein inclusions[44], in synaptic boutons (striatum, substantia nigra) and in cell body profiles in different brain regions of the mice in our study. We found a decrease of phospho-αSyn in the dorsal striatum of 2-HP-injected transgenic mice, possibly reflecting the structural neuronal injury induced in this region by 2-HP (Extended Data Fig 9a). We observed no significant effect in the SNpc, where a longer timespan between injection and analysis may be necessary to elicit an effect (Extended Data Fig 9b). Interestingly, in the prefrontal cortex, a brain region neuronally connected to the dorsal striatum, we observed a significant increase in the number of intracellular α-synuclein inclusions in 2-HP injected transgenic mice compared to their control counterparts (Extended Data Fig 9c).

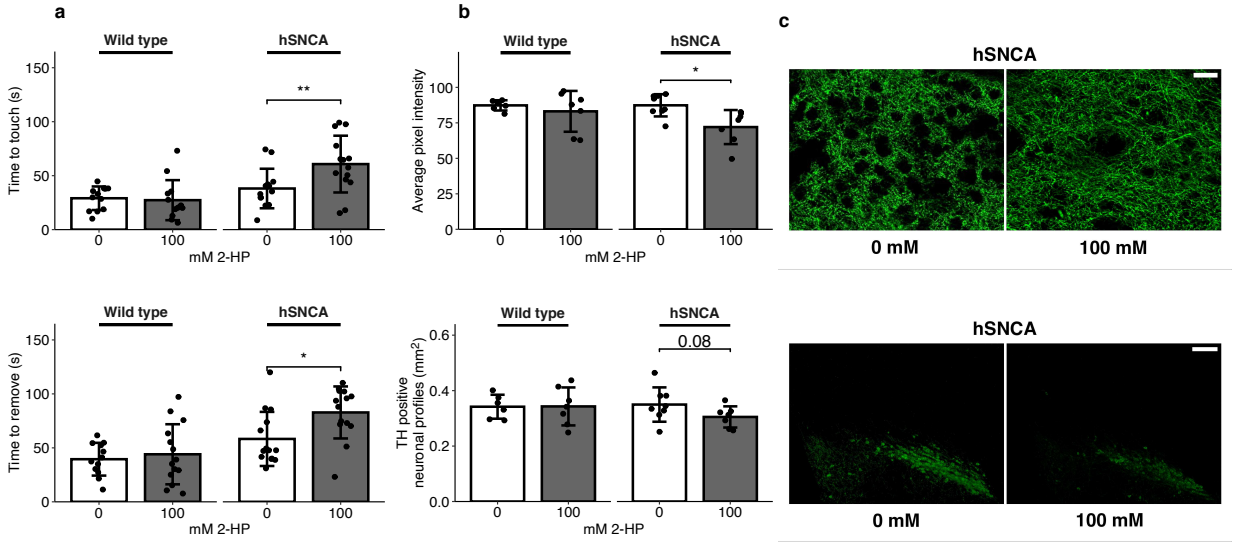

Figure 3. Effects of intrastriatally injected 2-hydroxypyridine on fine motor behaviour and the dopaminergic neuron marker tyrosine hydroxylase (TH) in transgenic mice overexpressing human α-synuclein. a. Fine motor behaviour of mice 2 months after 2-HP injection, measured using the adhesive removal test (time to touch: upper panel, time to remove: lower panel); hSNCA: human α-synuclein

overexpressing transgenic mice; n of mice = 12-14 per group. **b.** Quantification of TH-positive structures in the nigro-striatal circuit of hSNCA mice at 2 months after 100 mM 2-HP injection; Upper panel: TH-positive axons in the dorsal striatum; lower panel: TH-positive neurons in the substantia nigra pars compacta; n of mice = 6-8 per group. **c.** Microphotographs showing examples for 0 mM and 100mM in hSNCA mice only; upper panel: dorsal striatum (scale bar: 25 μm); lower panel: substantia nigra pars compacta (scale bar: 200 μm). All bar plots show mean and standard deviation. * $P < 0.05$, ** $P < 0.01$.

Discussion

In mammals, 2-HP is a known metabolite of pyridine[45]. While pyridine ring structures are commonly present in biological systems and in man-made compounds, such as drugs and pesticides, unsubstituted pyridine is not common in nature[46]. We initially hypothesized that the 2-HP we measured in faecal samples could originate from bacterial breakdown of the pesticide chlorpyrifos, where 2-HP is an established intermediate product[22]. However, we did not detect chlorpyrifos or other related compounds in our faecal metabolomic data. Instead, our results indicate an association of 2-HP and the archaeal species *Methanobrevibacter smithii* as well as methanogenesis-related genes on the metagenomic and metatranscriptomic level. Moreover, we found β-glutamate, which is also linked to archaeal metabolism[27] to be statistically significantly different between PD, iRBD, and healthy control samples. At present, there is no established biosynthetic pathway for 2-HP in *Methanobrevibacter smithii* or in any other organism, but many hydrogenotrophic methanogenic archaea produce a cofactor which has a 2-pyridone structure[28]. We detected 2-HP in methanoarchaeal cells, suggesting that there is a metabolic process that produces this compound.

Our results show that 2-HP has effects relevant to PD pathogenesis in several model systems: increased α-synuclein aggregation in a humanized yeast model and in human iPSC-derived enteric neurons and exacerbated behavioural symptoms and neuropathological changes in a mouse model

301 of PD. 2-HP has not been widely studied in mammals previously, and there are no reported
302 neurotoxic effects thus far. However, a ring-fused 2-pyridone compound (FN075) was shown to
303 increase α-synuclein aggregation through a mechanism that involves the formation of oligomers
304 with a flexible solvent-exposed C-terminal end; these oligomers then drive α-synuclein
305 fibrillation[32]. Injection of FN075 into the striatum or the substantia nigra of mice also causes PD-
306 like behavioural, metabolic and neuropathological changes, and these changes are absent in mice
307 that do not produce α-synuclein[47]. An analogous mechanism could explain our *in vitro* and *in vivo*
308 findings concerning 2-HP and α-synuclein.
309
310 We detected 2-HP at highest concentrations in faecal samples compared to plasma or CSF,
311 implicating the gut as a likely anatomic origin. This is in line with Braak's dual hit hypothesis[12],
312 which posits that in PD α-synuclein aggregation begins in the gut and spreads from the enteric
313 nervous system to the central nervous system. Furthermore, the presence of 2-HP in plasma,
314 combined with our prediction that it can likely pass the blood-brain barrier, represents another
315 potential route for spreading. We hypothesize that 2-HP could act together with other PD-
316 influencing microbial mechanisms. This would be parallel to the gut microbiome-dependent
317 process which has been described in mouse models of PD using the pesticide/insecticide rotenone,
318 administered via intrastriatal injections[48,49]. For example, intestinal barrier disruption due to mucus
319 erosion by *Akkermansia muciniphila*[50], a microbe that is often reported to be increased in PD
320 patients[3,13], could lead to increased exposure to harmful microbial metabolites, such as 2-HP
321 produced by *M. smithii*. This would then drive α-synuclein aggregation, initiating or exacerbating
322 PD pathogenesis. In this context, it has not escaped our attention that a mechanism involving *M.*

323 *smithii* represents a first known example for a clear role for archaea in a human disease
324 pathogenesis.
325

326 References

327 1. Benakis, C. *et al.* The microbiome-gut-brain axis in acute and chronic brain diseases. *Curr.*
328 *Opin. Neurobiol.* **61**, 1–9 (2020).
329 2. Boertien, J. M., Pereira, P. A. B., Aho, V. T. E. & Scheperjans, F. Increasing comparability
330 and utility of gut microbiome studies in Parkinson's disease: A systematic review. *J. Park.*
331 *Dis.* **9**, S297-S312 (2019).
332 3. Romano, S. *et al.* Meta-analysis of the Parkinson's disease gut microbiome suggests alterations
333 linked to intestinal inflammation. *npj Park. Dis.* **7**, 1–13 (2021).
334 4. Qian, Y. *et al.* Gut metagenomics-derived genes as potential biomarkers of Parkinson's
335 disease. *Brain* **143**, 2474–2489 (2020).
336 5. Rosario, D. *et al.* Systematic analysis of gut microbiome reveals the role of bacterial folate and
337 homocysteine metabolism in Parkinson's disease. *Cell Rep.* **34**, 108807 (2021).
338 6. Fang, P., Kazmi, S. A., Jameson, K. G. & Hsiao, E. Y. The microbiome as a modifier of
339 neurodegenerative disease risk. *Cell Host Microbe* **28**, 201–222 (2020).
340 7. Sung, H. *et al.* Global Cancer Statistics 2020: GLOBOCAN Estimates of incidence and
341 mortality worldwide for 36 cancers in 185 countries. *CA. Cancer J. Clin.* **71**, 209–249 (2021).
342 8. Matson, V., Chervin, C. S. & Gajewski, T. F. Cancer and the microbiome—Influence of the
343 commensal microbiota on cancer, immune responses, and immunotherapy. *Gastroenterology*
344 **160**, 600–613 (2021).

345 9. Fan, Y. & Pedersen, O. Gut microbiota in human metabolic health and disease. *Nat. Rev.*
346 *Microbiol.* **19**, 55–71 (2021).
347 10. Dorsey, E. R., Sherer, T., Okun, M. S. & Bloem, B. R. The emerging evidence of the Parkinson
348 pandemic. *J. Park. Dis.* **8**, S3–S8 (2018).
349 11. Miyauchi, E., Shimokawa, C., Steimle, A., Desai, M. S. & Ohno, H. The impact of the gut
350 microbiome on extra-intestinal autoimmune diseases. *Nat. Rev. Immunol.* 1–15 (2022)
351 doi:10.1038/s41577-022-00727-y.
352 12. Hawkes, C. H., Tredici, K. D. & Braak, H. Parkinson's disease: a dual-hit hypothesis.
353 *Neuropathol. Appl. Neurobiol.* **33**, 599–614 (2007).
354 13. Heintz-Buschart, A. *et al.* The nasal and gut microbiome in Parkinson's disease and idiopathic
355 rapid eye movement sleep behavior disorder. *Mov. Disord.* **33**, 88–98 (2018).
356 14. Högl, B., Stefani, A. & Videnovic, A. Idiopathic REM sleep behaviour disorder and
357 neurodegeneration — an update. *Nat. Rev. Neurol.* **14**, 40–55 (2018).
358 15. Unger, M. M. *et al.* Short chain fatty acids and gut microbiota differ between patients with
359 Parkinson's disease and age-matched controls. *Parkinsonism Relat. Disord.* **32**, 66–72 (2016).
360 16. Aho, V. T. E. *et al.* Relationships of gut microbiota, short-chain fatty acids, inflammation, and
361 the gut barrier in Parkinson's disease. *Mol. Neurodegener.* **16**, (2021).
362 17. Baldini, F. *et al.* Parkinson's disease-associated alterations of the gut microbiome predict
363 disease-relevant changes in metabolic functions. *BMC Biol.* **18**, 62 (2020).
364 18. Heintz-Buschart, A. & Wilmes, P. Human gut microbiome: Function matters. *Trends*
365 *Microbiol.* **26**, 563–574 (2018).
366 19. Roume, H. *et al.* A biomolecular isolation framework for eco-systems biology. *ISME J.* **7**,
367 110–121 (2013).

368 20. Heintz-Buschart, A. *et al.* Integrated multi-omics of the human gut microbiome in a case study
369 of familial type 1 diabetes. *Nat. Microbiol.* **2**, 1–13 (2016).
370 21. Kopka, J. *et al.* GMD@CSB.DB: the Golm Metabolome Database. *Bioinformatics* **21**, 1635–
371 1638 (2005).
372 22. Uniyal, S., Sharma, R. K. & Kondakal, V. New insights into the biodegradation of chlorpyrifos
373 by a novel bacterial consortium: Process optimization using general factorial experimental
374 design. *Ecotoxicol. Environ. Saf.* **209**, 111799 (2021).
375 23. Freire, C. & Koifman, S. Pesticide exposure and Parkinson's disease: Epidemiological
376 evidence of association. *NeuroToxicology* **33**, 947–971 (2012).
377 24. Mohammadzadeh, R., Mahnert, A., Duller, S. & Moissl-Eichinger, C. Archaeal key-residents
378 within the human microbiome: characteristics, interactions and involvement in health and
379 disease. *Curr. Opin. Microbiol.* **67**, 102146 (2022).
380 25. Vandeputte, D. *et al.* Stool consistency is strongly associated with gut microbiota richness and
381 composition, enterotypes and bacterial growth rates. *Gut* **65**, 57–62 (2016).
382 26. Warnecke, T., Schäfer, K.-H., Claus, I., Del Tredici, K. & Jost, W. H. Gastrointestinal
383 involvement in Parkinson's disease: pathophysiology, diagnosis, and management. *npj Park.*
384 *Dis.* **8**, 1–13 (2022).
385 27. Robinson, P., Neelon, K., Schreier, H. J. & Roberts, M. F. β-glutamate as a substrate for
386 glutamine synthetase. *Appl. Environ. Microbiol.* **67**, 4458–4463 (2001).
387 28. Schick, M. *et al.* Biosynthesis of the iron-guanylylpyridinol cofactor of [Fe]-hydrogenase in
388 methanogenic archaea as elucidated by stable-isotope labeling. *J. Am. Chem. Soc.* **134**, 3271–
389 3280 (2012).

390 29. Li, H. *et al.* Effect of selection of molecular descriptors on the prediction of blood-brain barrier
391 penetrating and nonpenetrating agents by statistical learning methods. *J. Chem. Inf. Model.* **45**,
392 1376–1384 (2005).
393 30. Lee, S. K. *et al.* The PreADME Approach: Web-based program for rapid prediction of physico-
394 chemical, drug absorption and drug-like properties. *EuroQSAR 2002 Des. Drugs Crop Prot.*
395 *Process. Probl. Solut.* **2003**, 418–420 (2003).
396 31. Liu, H. *et al.* AlzPlatform: An Alzheimer's disease domain-specific chemogenomics
397 knowledgebase for polypharmacology and target identification research. *J. Chem. Inf. Model.*
398 **54**, 1050–1060 (2014).
399 32. Horvath, I. *et al.* Mechanisms of protein oligomerization: Inhibitor of functional amyloids
400 templates α-synuclein fibrillation. *J. Am. Chem. Soc.* **134**, 3439–3444 (2012).
401 33. Burré, J., Sharma, M. & Südhof, T. C. Cell biology and pathophysiology of α-synuclein. *Cold*
402 *Spring Harb. Perspect. Med.* **8**, (2018).
403 34. Willingham, S., Outeiro, T. F., DeVit, M. J., Lindquist, S. L. & Muchowski, P. J. Yeast genes
404 that enhance the toxicity of a mutant huntingtin fragment or α-synuclein. *Science* **302**, 1769–
405 1772 (2003).
406 35. Fanning, S. *et al.* Lipidomic analysis of α-synuclein neurotoxicity identifies stearoyl CoA
407 desaturase as a target for Parkinson treatment. *Mol. Cell* **73**, 1001-1014.e8 (2019).
408 36. Su, L. J. *et al.* Compounds from an unbiased chemical screen reverse both ER-to-Golgi
409 trafficking defects and mitochondrial dysfunction in Parkinson's disease models. *Dis. Model.*
410 *Mech.* **3**, 194–208 (2010).
411 37. Vincent, B. M. *et al.* Inhibiting stearoyl-CoA desaturase ameliorates α-synuclein cytotoxicity.
412 *Cell Rep.* **25**, 2742-2754.e31 (2018).

413 38. Mazzulli, J. R., Zunke, F., Isacson, O., Studer, L. & Krainc, D. α-Synuclein–induced lysosomal
414 dysfunction occurs through disruptions in protein trafficking in human midbrain
415 synucleinopathy models. *Proc. Natl. Acad. Sci. U. S. A.* **113**, 1931–1936 (2016).
416 39. Fattahi, F. *et al.* Deriving human ENS lineages for cell therapy and drug discovery in
417 Hirschsprung's disease. *Nature* **531**, 105–109 (2016).
418 40. Garcia, P. *et al.* Neurodegeneration and neuroinflammation are linked, but independent of
419 alpha-synuclein inclusions, in a seeding/spreading mouse model of Parkinson's disease. *Glia*
420 (2022) doi:10.1002/glia.24149.
421 41. Luk, K. C. *et al.* Pathological α-synuclein transmission initiates Parkinson-like
422 neurodegeneration in nontransgenic mice. *Science* **338**, 949–953 (2012).
423 42. Desbène, C. *et al.* Critical role of cPLA2 in Aβ oligomer-induced neurodegeneration and
424 memory deficit. *Neurobiol. Aging* **33**, 1123.e17–29 (2012).
425 43. Bouet, V. *et al.* The adhesive removal test: a sensitive method to assess sensorimotor deficits
426 in mice. *Nat. Protoc.* **4**, 1560–1564 (2009).
427 44. Vaikath, N. N. *et al.* Antibodies against alpha-synuclein: tools and therapies. *J. Neurochem.*
428 **150**, 612–625 (2019).
429 45. Damani, L. A. *et al.* Species differences in the metabolic *C* - and *N* -oxidation, and *N* -
430 methylation of [^{14}C]pyridine *in vivo*. *Xenobiotica* **12**, 527–534 (1982).
431 46. Gupta, N., O'Loughlin, E. J. & Sims, G. K. Microbial degradation of pyridine and pyridine
432 derivatives. in *Microbial Metabolism of Xenobiotic Compounds* (ed. Arora, P. K.) vol. 10 1–
433 31 (Springer Singapore, 2019).
434 47. Chermenina, M. *et al.* Single injection of small-molecule amyloid accelerator results in cell
435 death of nigral dopamine neurons in mice. *npj Park. Dis.* **1**, 15024 (2015).

436 48. Dodiya, H. B. *et al.* Chronic stress-induced gut dysfunction exacerbates Parkinson's disease
437 phenotype and pathology in a rotenone-induced mouse model of Parkinson's disease.
438 *Neurobiol. Dis.* **135**, 104352 (2020).
439 49. Perez-Pardo, P. *et al.* Role of TLR4 in the gut-brain axis in Parkinson's disease: a translational
440 study from men to mice. *Gut* **68**, 829–843 (2019).
441 50. Desai, M. S. *et al.* A dietary fiber-deprived gut microbiota degrades the colonic mucus barrier
442 and enhances pathogen susceptibility. *Cell* **167**, 1339-1353.e21 (2016).
443

444 Methods

445 Patient cohorts and sampling

446 Individuals with PD (n = 50) or iRBD (n = 30) and healthy control subjects (n = 50) were recruited
447 from two study sites in Germany (Paracelsus-Elena Klinik, Kassel, and Philipps-University,
448 Marburg). The studies conformed to the Declaration of Helsinki and the ethical guidelines of the
449 respective institutions (Kassel: approved by the ethics committee of the Physician's Board Hessen,
450 Germany (FF 89/2008), and the DeNoPa trial registered at the German Register for Clinical trials
451 (DRKS00000540); Marburg: approved by the ethics committee of the Medical Faculty of the
452 Philipps-University, Marburg, Germany (46/14)). All subjects provided informed written consent.
453 The sample analysis was approved by the Comité National d'Ethique de Recherche of
454 Luxembourg (reference no.: 140174_ND). For the targeted validation measurements of our main
455 metabolomics finding, we used a set of DeNoPa cohort samples consisting of 25 later-time point
456 samples from individuals included in the main multi-omic analyses, and 35 samples from

457 previously unmeasured individuals. Further details on recruitment, inclusion and exclusion criteria
458 and clinical data collection are provided in the Supplementary .
459
460 For both cohorts, faecal samples were collected at the clinic via a stool specimen collector
461 (MedAuxil) and collection tubes (Sarstedt), as previously described[13]. Samples were immediately
462 flash-frozen on dry ice after collection. Samples were subsequently stored at –80 °C and shipped
463 on dry ice. For the Kassel cohort, blood and cerebrospinal fluid samples were also obtained, as
464 described previously[51].
465
466 Extractions from faecal samples were performed according to a previously published protocol[19,52],
467 conducted on a customized robotic system (Tecan Freedom EVO 200). After exclusions, the final
468 sample set consisted of samples from 46 PD and 27 iRBD cases and 49 control subjects; see
469 Supplementary for additional details.
470

471 Metagenomic and metatranscriptomic sequencing

472 For metagenomics, all DNA samples were subjected to random shotgun sequencing. Following
473 DNA isolation, 200-300 ng of DNA was sheared using a Bioruptor NGS (Diagenode) with 30s
474 ON and 30s OFF for 20 cycles. Sequencing libraries were prepared using the TruSeq Nano DNA
475 library preparation kit (Illumina) following the manufacturer's protocol, with 350 bp average insert
476 size.
477
478 For metatranscriptomics, 1 µg of isolated RNA was rRNA-depleted using the RiboZero kit
479 (Illumina, MRZB12424). Library preparation was performed using the TruSeq Stranded mRNA

480 library preparation kit (Illumina) following the manufacturer's protocol, apart from omitting the
481 initial steps for mRNA pull down.
482
483 For metagenomic and metatranscriptomic analyses, the qualities of the libraries were checked
484 using a Bioanalyzer (Agilent) and quantified using Qubit (Invitrogen). Libraries were sequenced
485 on an Illumina NextSeq500 instrument with 2x150 bp read length.
486

487 **Metaproteomics**

488 Following isolation, 20 µl of protein extracts were processed using the paramagnetic bead
489 approach with SP3 carboxylate coated beads[53,54]; further details are provided in the Supplementary
490 . The resulting peptide lysates were analysed on a Q Exactive HF instrument (Thermo Fisher
491 Scientific) equipped with a TriVersa NanoMate source (Advion) in LC chip coupling mode.
492 Peptide lysates were injected on a trapping column (Acclaim PepMap 100 C18, 3 µm, nanoViper,
493 75 µm x 2 cm, Thermo Fisher Scientific) with 5 µL/min by using 98% water/2% ACN 0.5%
494 trifluoroacetic acid, and separated on an analytical column (Acclaim PepMap 100 C18, 3 µm,
495 nanoViper, 75 µm x 25 cm, Thermo Fisher Scientific) with a flow rate of 300 nl/min. The mobile
496 phase was comprised of 0.1% formic acid in water (A) and 80 % ACN/0.08 % formic acid in water
497 (B). Full MS spectra (350–1,550 m/z) were acquired in the Orbitrap at a resolution of 120,000 with
498 automatic gain control (AGC) and a target value of 3×10^6 ions.
499

500 **Metabolomics**

501 Untargeted GC-MS and SCFA measurements from faecal samples were performed according to a
502 previously published protocol[52]. Details for untargeted LC-MS/MS measurements from faecal
503 samples are provided in the Supplementary .
504
505 For targeted 2-HP detection in faecal samples, polar metabolites were extracted as follows: 500
506 µL of MilliQ water was added to 50 mg of faecal matter. Samples were homogenized using a
507 Precellys24 homogenizer (Bertin Technologies): 6000 rpm, 1*x*30 s at 0 to 5 °C. Plasma and CSF
508 as well as further sample preparation of samples and measurement parameters were performed as
509 previously described[55]. For unambiguous identification and precise quantification of 2-HP,
510 concentrations were determined using a standard addition approach. Aliquots of the same sample
511 (faecal sample, plasma or CSF, with added internal standards: pentanedioic acid-D6, [U-^{13}C]-
512 ribitol and tridecanoic acid-D25) were separately spiked with different concentrations of 2-HP (10,
513 50, 100, 150 and 200 µmol/l) to extrapolate compound levels. Derivatization and GC-MS
514 measurements were performed as reported before.
515
516 All GC-MS chromatograms were processed using MetaboliteDetector, v3.220190704[56].
517 Compounds were initially annotated by retention time and mass spectrum using an in-house mass
518 spectral library. Internal standards were added at the same concentration to every medium sample
519 to correct for uncontrolled sample losses and analyte degradation during metabolite extraction.
520 The data was normalized by using the response ratio of the integrated peak area of the analyte and
521 the integrated peak area of the internal standard.
522

523 **Bioinformatics and statistics for multi-omics**

524 Metagenomic and metatranscriptomic sequencing data were analysed using the IMP pipeline,
525 version 01.07.2020 (https://git-r3lab.uni.lu/IMP/imp3, tag 6f1badf7), using the HPC facilities[57] of
526 the University of Luxembourg. Metagenomic and metatranscriptomic reads were quality-
527 controlled and co-assembled, ORFs predicted, reads and contigs taxonomically annotated, and
528 ORFs functionally annotated as previously described[58]. Protein libraries were generated from the
529 IMP output and used for protein identification on a per sample basis using SearchGUI[59] (v. 3.3.20).
530 Further details are provided in the Supplementary .
531
532 All statistical analyses and visualizations were performed in R[60] (v. 4.1.0) using targets[61] (v. 0.8.1)
533 for workflow management and knitr[62–64] (v. 1.36) for reporting. Unless otherwise specified, false
534 discovery rates were used for multiple comparison correction. Differential abundance comparisons
535 were performed with DESeq2[65] (v. 1.32.0; adjusted for age and sex) for metagenomic and
536 metatranscriptomic data, and with ANOVA (adjusted for age and sex) and two-sided t-tests (not
537 corrected for confounders) for the metabolomic and metaproteomic data. Integrated multi-omic
538 testing was implemented with the DIABLO workflow from mixOmics[66] (v. 6.17.29). Additional
539 details are provided in the Supplementary .
540

541 **2-HP detection in methanoarchaeal cultures**

542 The archaea *Methanosarcina mazei* (DSM #3647) *and Methanobrevibacter smithii* (DSM #861)
543 were cultivated under anaerobic conditions in closed serum bottles containing 50 mL minimal
544 medium complemented with 1 mM sodium sulphide, 2 mM cysteine and ampicillin to avoid

545 bacterial contamination[67]. As carbon and energy sources, 150 mM methanol for *M. mazei* and
546 H_2/CO_2 (80:20) in the gas atmosphere for *M. smithii* were added. Cultures were incubated at 37
547 °C. For monitoring growth, the turbidity at 600 nm was measured using an Ultraspec 2100 Pro
548 Photometer (Amersham Biosciences). Cell numbers were determined in parallel using a Thoma
549 cell counting chamber. Cells were harvested in mid and late exponential phase by centrifugation
550 at 2,455 x g for 20 min at 4 °C. The cell pellets were resuspended in 0.9 % sodium chloride solution
551 and centrifuged again (21,130 x g, 10 min, 4°C). All samples were stored at -80 °C. 2-HP was
552 measured using targeted GC-MS, with sample quantities normalized for cell counts; full details
553 are provided in the Supplementary .
554

555 **Yeast model**

556 The human *SNCA* gene was cloned into pAG306GAL-ccdB-EGFP and pAG304GAL-ccdB-EGFP
557 plasmids using the Gateway cloning system[68]. Yeast cells were transformed with the constructs
558 using the standard polyethylene glycol/lithium acetate protocol[69]. The *PDR*5 gene was
559 subsequently replaced by *URA3* marker in the HiTox and control strains followed by selection in
560 synthetic complement (SC) media lacking uracil using the same transformation protocol[69]. Gene
561 integration or disruption was verified by PCR. Strain details are provided in the Supplementary .
562

563 Four fresh single colonies of the HiTox strain and its respective control strain were inoculated
564 from SC-2% glucose plates into 5 mL SC-2% raffinose (SCR) and incubated overnight with
565 shaking (200 rpm) at 30 °C for 20 h. Cultures were subsequently diluted to OD 0.5 and 2 µL of
566 culture was added to 78 µL 2-HP containing media to a final optical density of 0.0125 in a 384-
567 well microplate. 2-HP was diluted in SC-2% raffinose/galactose (SCR/SCG) and tested at different

568 concentrations (1-100 mM). Finally, plates were measured in a microplate reader (TECAN™
569 Infinite M200Pro), at an interval of 10 minutes during 72 h at 30 °C. Yeast growth phenotyping
570 was performed as previously described[74]. For better comparability between batches, strains and
571 methods, the final biomass was corrected using the GATHODE software[70]. The OD600 at 48 h
572 was recorded for biomass quantification, with the means and standard deviations calculated from
573 four biological replicates.
574
575 To evaluate α-synuclein aggregation, one single colony was inoculated in 5 mL SCR (α-syn 'off')
576 and incubated at 30 °C overnight. The following day, 1 mL of culture was transferred into an
577 sample tube and cells were centrifuged. Pellets were resuspended with SCG (α-syn 'on') in
578 presence or absence of 30 mM 2-HP and incubated at 30 °C. After 24 h, cells were visualized using
579 a Nikon Microscope (100x oil). Ten pictures per condition were randomly taken. The total number
580 of cells and cells showing aggregates were manually quantified in ImageJ. Statistical significance
581 between conditions was determined using an unpaired two-sided t-test in R.
582

583 **Enteric neuron model**

584 Enteric neurons were derived from human induced pluripotent stem cells (hiPSCs) following a
585 previously published protocol[39]; the full details are available in the Supplementary Methods.
586
587 For cytotoxicity testing, enteric neurons were detached with accutase (Sigma) after 21 days of
588 culturing in 6-well plates. The cells were replated into 96-well plates coated with poly-
589 ornithine/laminin/fibronectin as described in the Supplementary methods. They were then
590 maintained under differentiating conditions until day 31, when they were treated with 2-HP

591 (Sigma,) at 1 μM, 3 μM, 6 μM, 10 μM, 30 μM, 60 μM, 100 μM, 300 μM, 600 μM, 1 mM and 3
592 mM. 2-HP was reconstituted to 10 mM in the differentiation medium. Cells were treated for 24h,
593 then assessed using a tetrazolium assay for viability; see Supplementary Methods for details.
594
595 For immunostaining, enteric neurons were replated into 96-well imaging plates (Cell Carrier Ultra,
596 Perkin Elmer) after three weeks in culture. Cells were maintained under differentiating conditions
597 until day 31, when they were treated with 60 μM 2-HP for 72 h and 120 h. After treatment, cells
598 were immunostained with α-synuclein antibody (NOVUS biologicals, NBP1-05194, 1:1000), α-
599 synuclein filament antibody (Abcam, ab20953, 1:5000), TUJ1 (Millipore, AB9354, 1:600) and
600 cleaved caspase-3 (Asp175) antibody (CST, 9661, 1:200) and imaged to quantify each marker (full
601 details in the Supplementary Methods). Differences were evaluated using one-way ANOVA with
602 the mean values of three independent replicates and a two-sided Dunn's multiple comparison test
603 at each time point versus the untreated using Graphpad Prism (v. 9).
604

605 **Mouse model**

606 A transgenic mouse line, B6.D2-Tg(Thy1-SNCA)14Pjk (Line 14), which overexpresses human
607 wildtype α-synuclein under the transcriptional control of the Thy1 promoter, was used[71,72].
608 Genotyping of the mice is described in the Supplementary Methods. The mice were all
609 heterozygous for the transgene, males, and 2-3 months old. Between 6 and 14 mice were used for
610 each analysis. Mice had access to food and water *ad libitum* and were exposed to a regular 12h-
611 day-night cycle. Mice were injected intracranially with 100 mM 2-HP (Sigma), or PBS vehicle
612 solution (control mice), in volumes of 2 μL, within the right dorsal striatum; full details of the
613 injection protocol are provided in the Supplementary Methods.

614

615 At two months post-injection, motor function was evaluated with the adhesive removal test[43].
616 Briefly, animals were placed in a round transparent arena for one minute for habituation.
617 Rectangular white tape, 3 *x* 5 mm was placed on the left forepaw (expected to be affected by
618 injection of 2-HP into the right dorsal striatum). The time intervals to first touch and removal of
619 the tape were recorded. The test was performed twice, sequentially, for each mouse, and times for
620 both measures were averaged. The sequence of the mice being tested was randomized, and the
621 experimenter was blinded to their genotype and treatment.

622

623 After behavioural evaluation, the mice were deeply anesthetised (i.p. injection of medetomidine,
624 1mg/kg and ketamine, 100 mg/kg) and then euthanised by transcardial perfusion with PBS. Brains
625 were removed from the skull and post-fixed in fresh phosphate-buffered 4% paraformaldehyde for
626 48 h at 4 °C, then stored in PBS with 0.05% sodium azide (as a preservative) at 4 °C, before being
627 processed for immunofluorescence analysis.

628

629 Immunofluorescent stainings on 50 µm sections, generated with a Leica VT 100 vibratome, were
630 performed following a standard protocol[73]. Briefly, sections were first washed in PBS with 0.1%
631 Triton X100 (T_{X100}). They were subsequently treated with a permeabilization solution (PBS +
632 1.5% T_{X100} + 3% H_2O_2) for 30 minutes. This was followed by washing with PBS + 0.1% T_{X100}.
633 To prevent unspecific antibody binding, the sections were then incubated for 1 h in PBS + 0.1%
634 T_{X100} with 5% BSA. After one short washing step, sections were incubated with the first antibodies
635 diluted in antibody solution (PBS + 0.1% T_{X100} + 2% BSA) overnight at room temperature (RT)
636 on an orbital shaker. The following antibodies were used: anti-α-synuclein (aSyn, phosphorylated

637 at S129; Prothena Biosciences Inc., 11A5; 1:1000), anti-tyrosine hydroxylase (TH; Abcam,
638 ab76442/Merck (Sigma-Aldrich), AB152; 1:1000). The sections were double-stained for TH and
639 S129 phosphorylated α-synuclein (phospho-αSyn). The next day, sections were washed with PBS
640 + 0.1% T_{X100} to remove any excess of the first antibody. Sections were then incubated with a
641 secondary antibody in antibody solution for 2 h at RT on an orbital shaker. Finally, sections were
642 washed with PBS + 0.1% T_{X100} (at least 3 times for 10 mins), then mounted on Superfrost™
643 (ThermoFisher Scientific) slides, left to dry, and finally covered with a cover-slip using
644 Fluoromount-G® (Invitrogen).
645
646 Imaging of the sections was performed using a Zeiss AxioImager Z1 upright microscope, coupled
647 to a "Colibri" LED system, and an Mrm3 digital camera for image capture using the Zeiss ZEN 2
648 Blue software. Measurements were performed on blinded sections, and codes were broken only
649 after all measurements were completed. TH-positive signals were quantified in the dorsal striatum
650 and substantia nigra pars compacta, and phospho-aSyn in these two regions as well as the
651 prefrontal cortex; details of the quantifications for each region and antibody are given in the
652 Supplementary Methods.
653
654 Behaviour and neuropathology data were analysed with Graphpad Prism (v. 9). All datasets passed
655 normality tests and were analysed by ANOVA followed by Tukey's or Dunn's post hoc tests.
656
657 The animal study was approved by the University of Luxembourg Animal Experimentation Ethics
658 Committee (LUPA 2020/26) and the overseeing Luxembourg Government authorities (Ministry
659 of Health and Ministry of Agriculture).

660 # Data availability

661 The datasets generated by this study are available in the following repositories: metagenomic and
662 metatranscriptomic data at the NCBI BioProject collection with the ID PRJNA782492
663 (http://www.ncbi.nlm.nih.gov/bioproject/782492), metaproteomic data at the Proteomics
664 Identifications (PRIDE) database with accession number PXD031457
665 (https://www.ebi.ac.uk/pride/archive/projects/PXD031457), and metabolomic data at
666 MetaboLights with ID MTBLS5092 (https://www.ebi.ac.uk/metabolights/MTBLS5092). Due to
667 privacy restrictions, clinical and demographic data are available on request from the corresponding
668 author. NCER-PD clinical and 16S rRNA amplicon sequencing data are available on request from
669 https://www.parkinson.lu/research-participation.

670

671 # Code availability

672 The IMP pipeline, which was used for analysis of metagenomic and metatranscriptomic data, is
673 available at https://gitlab.lcsb.uni.lu/IMP/imp3. The R code used for statistical analyses and
674 visualisations is available at https://gitlab.lcsb.uni.lu/ESB/mibipa-2-hp.

675

676 # Methods references

677 51. Mollenhauer, B. *et al.* Monitoring of 30 marker candidates in early Parkinson disease as
678 progression markers. *Neurology* **87**, 168–177 (2016).
679 52. Hughes, C. S. *et al.* Single-pot, solid-phase-enhanced sample preparation for proteomics
680 experiments. *Nat. Protoc.* **14**, 68–85 (2019).
681 53. Bannuscher, A. *et al.* A multi-omics approach reveals mechanisms of nanomaterial toxicity
682 and structure–activity relationships in alveolar macrophages. *Nanotoxicology* **14**, 181–195
683 (2020).
684 54. De Saedeleer, B. *et al.* Systematic characterization of human gut microbiome-secreted
685 molecules by integrated multi-omics. *ISME Commun.* **1**, 1–6 (2021).
686 55. Glaab, E. *et al.* Integrative analysis of blood metabolomics and PET brain neuroimaging data
687 for Parkinson's disease. *Neurobiol. Dis.* **124**, 555–562 (2019).
688 56. Hiller, K. *et al.* MetaboliteDetector: Comprehensive analysis tool for targeted and nontargeted
689 GC/MS based metabolome analysis. *Anal. Chem.* **81**, 3429–3439 (2009).
690 57. Varrette, S., Bouvry, P., Cartiaux, H. & Georgatos, F. Management of an academic HPC
691 cluster: The UL experience. in *2014 International Conference on High Performance*
692 *Computing Simulation (HPCS)* 959–967 (2014). doi:10.1109/HPCSim.2014.6903792.
693 58. Narayanasamy, S. *et al.* IMP: a pipeline for reproducible reference-independent integrated
694 metagenomic and metatranscriptomic analyses. *Genome Biol.* **17**, (2016).
695 59. Barsnes, H. & Vaudel, M. SearchGUI: A highly adaptable common interface for proteomics
696 search and de novo engines. *J. Proteome Res.* **17**, 2552–2555 (2018).
697 60. Team, R. C. *R: A language and environment for statistical computing*. (R Foundation for
698 Statistical Computing, 2021).

699 61. Landau, W. M. The targets R package: a dynamic Make-like function-oriented pipeline toolkit
700 for reproducibility and high-performance computing. *J. Open Source Softw.* **6**, 2959 (2021).
701 62. Xie, Y. *knitr: A General-Purpose Package for Dynamic Report Generation in R*. (2021).
702 63. Xie, Y. *Dynamic Documents with R and knitr*. (Chapman and Hall/CRC, 2015).
703 64. Xie, Y. knitr: A Comprehensive Tool for Reproducible Research in R. in *Implementing*
704 *Reproducible Computational Research* (eds. Stodden, V., Leisch, F. & Peng, R. D.) (Chapman
705 and Hall/CRC, 2014).
706 65. Love, M. I., Huber, W. & Anders, S. Moderated estimation of fold change and dispersion for
707 RNA-seq data with DESeq2. *Genome Biol.* **15**, 550 (2014).
708 66. Rohart, F., Gautier, B., Singh, A. & Le Cao, K.-A. mixOmics: An R package for 'omics feature
709 selection and multiple data integration. *PLoS Comput. Biol.* **13**, e1005752 (2017).
710 67. Ehlers, C., Veit, K., Gottschalk, G. & Schmitz, R. A. Functional organization of a single nif
711 cluster in the mesophilic archaeon Methanosarcina mazei strain Gö1. *Archaea* **1**, 143–150
712 (2002).
713 68. Alberti, S., Gitler, A. D. & Lindquist, S. A suite of Gateway® cloning vectors for high-
714 throughput genetic analysis in Saccharomyces cerevisiae. *Yeast Chichester Engl.* **24**, 913–919
715 (2007).
716 69. Gietz, R. D. & Woods, R. A. Transformation of yeast by lithium acetate/single-stranded carrier
717 DNA/polyethylene glycol method. *Methods Enzymol.* **350**, 87–96 (2002).
718 70. Jung, P. P., Christian, N., Kay, D. P., Skupin, A. & Linster, C. L. Protocols and programs for
719 high-throughput growth and aging phenotyping in yeast. *PLoS ONE* **10**, (2015).
720 71. Kahle, P. J. *et al.* Selective insolubility of α-synuclein in human Lewy body diseases Is
721 recapitulated in a transgenic mouse model. *Am. J. Pathol.* **159**, 2215–2225 (2001).

722 72. Kahle, P. J. *et al.* Subcellular localization of wild-type and Parkinson's disease-associated
723 mutant α-synuclein in human and transgenic mouse brain. *J. Neurosci.* **20**, 6365–6373 (2000).
724 73. Ashrafi, A. *et al.* Absence of regulator of G-protein signaling 4 does not protect against
725 dopamine neuron dysfunction and injury in the mouse 6-hydroxydopamine lesion model of
726 Parkinson's disease. *Neurobiol. Aging* **58**, 30–33 (2017).
727

728 Acknowledgements

729 We thank the staff of the Luxembourg Centre for Systems Biomedicine (LCSB), particularly the
730 sequencing platform and the metabolomics platform, for running the sequencing and metabolomic
731 analyses. The microscopy for the yeast experiments was performed at the LCSB bio-imaging
732 platform. The bioinformatics presented in this paper were carried out using the HPC facilities[57] of
733 the University of Luxembourg.
734
735 This project has received funding from the European Research Council (ERC) under the European
736 Union's Horizon 2020 research and innovation programme (grant agreement No. 863664), and
737 was further supported by the Luxembourg National Research Fund (FNR)
738 CORE/16/BM/11333923 (MiBiPa) and CORE/15/BM/10404093 (microCancer/MUST), and the
739 Michael J. Fox Foundation under grant IDs 14701 (MiBiPa-PLUS) and MJFF-019228
740 (PARKdiet), as well as the Parkinson's Foundation (MiBiPa Saliva), to P.W.
741
742 K.J.S. is a recipient of an FNR pre-doctoral fellowship (FNR AFR 12515776). A.S. is supported
743 by PARK-QC DTU (PRIDE17/12244779/PARK-QC), and B.T.A. by MICROH DTU

744 (PRIDE17/11823097). C.L.L. acknowledges funding support to U.H.-M. by the FNR CORE grant
745 (C20/BM/14701042). E.L.S. acknowledges funding support for the ATTRACT Fellowship
746 A18/BM/12341006. The work of R.A.S. was conducted with financial support of the DFG as part
747 of the CRC1182 “Origin and function of metaorganisms" Z2 project. E.G. acknowledges support
748 by the FNR as part NCER-PD (FNR11264123), the ERA-Net ERACOSySMed JTC-2 project PD-
749 Strat (INTER/11651464), and from the European Union’s Horizon 2020 research and innovation
750 programme under the grant no. ERAPERMED 2020-314 for the project DIGI-PD. P.M. was
751 supported by the FNR funded National Centre of Excellence in Research on Parkinson’s disease
752 (NCER-PD, FNR11264123), CORE MiRisk-PD (C17/BM/11676395), and the INTER
753 ‘ProtectMove’ (INTER/DFG/19/1442937) grants. Finally, the authors thank Prof. Michel
754 Mittelbronn, who is funded by a PEARL grant (FNR PEARL P16/BM/11192868), as well as the
755 Jean Think Foundation, Luxembourg, for their support.
756

757 Author information

758 These authors contributed equally: Jean-Pierre Trezzi, Velma T. E. Aho.
759

760 Contributions

761 Conceptualisation: J.-P.T., A.H.-B., W.O., B.M., P.W. Patient recruitment, clinical coordination,
762 and sampling: S.S., A.J., C.T., W.O., B.M. Project management: L.D., C.C.L. Multi-omic data
763 generation: J.-P.T., C.J., R.H., R.R.S., B.T.A., L.A.L., A.D., J.H., X.D., F.G., N.J., M.v.B., E.L.S.
764 Bioinformatics and statistics: J.-P.T., V.T.E.A, C.J., O.H., B.K., P.V.N., J.R.-G., R.R.S., B.T.A.,
765 E.L.S., E.G., A.H.-B., P.M. Experimental work: M.H.T., K.J.S., P.G., A.S., C.M-G., O.U.H., T.H.,

766 U.H.-M., G.G.-G., K.W., R.A.S., J.C.S., C.L.L., T.K., M.B., Initial manuscript draft: J.-P.T.,
767 V.T.E.A, P.W. Extensive review and editing: C.C.L., A.H.-B., J.G.S. All authors read and
768 approved of the submitted version.
769

770 Ethics declarations

771 Competing interests

772 J.-P.T. and P.W. are inventors in patent applications involving the discoveries described in this
773 publication: 1) No. LU101477, No. PCT/EP2020/081855, EP20820786.0, US17/776,001,
774 CA3,157,474; 2) No. LU101476, No. PCT/EP2020/081832, EP20820785.2, US17/776,010, filed
775 by the University of Luxembourg. V.T.E.A. is an inventor in the following patents which concern
776 the use of microbes in the diagnosis and treatment of Parkinson's disease: FI127671B,
777 EP3149205B1 and US10139408B2 (issued); US20190137493A1, US20210109098A1 and
778 EP3789501A1 (pending); these patents are currently assigned to NeuroBiome Ltd. W.O. is the
779 president of the European Brain Council. P.W. and B.M. are members of the scientific steering
780 committee for a clinical trial by 4D Pharma. The rest of the authors declare no competing interests.
781

782 Additional information

783 Supplementary information

784 Supplementary information is available for this paper.

785 **Corresponding author**

786 Correspondence should be addressed to Paul Wilmes (paul.wilmes@uni.lu).

787

788 Extended data figures and tables

789 **Extended Data Figure 1.** Multi-omic data analysis workflow. PD = Parkinson's disease, iRBD =
790 idiopathic REM sleep behaviour disorder, Ctrl = control subject.

791 **Extended Data Table 1. Demographic and clinical data on study subjects.** a. Main multi-omic
792 analyses, b. 2-HP targeted validation, c. NCER-PD cohort (16S rRNA gene amplicons).

793 **Extended Data Figure 2. Independent Principal Component Analysis (IPCA) for each data**
794 **type.** Testing was performed separately for each data type, with total number of components
795 chosen based on kurtosis. The first two components are shown for each data type regardless of
796 total number of components. In the 1st column, green triangles and dashed line correspond to
797 control subjects, and black circles and solid line to patients with PD or iRBD. Ellipses reflect 95%
798 confidence. 2nd and 3rd columns show 10 features with the highest loadings. a. Untargeted
799 metabolomics; showing 2/2 components, b. Taxonomically classified metagenomic reads; 2/3
800 components, c. Taxonomically classified metatranscriptomic reads; 2/2 components, d.
801 Taxonomically classified metaproteomic spectra; 2/4 components, e. Functionally classified
802 (KEGG orthologs; KOs) metagenomic reads; 2/3 components, f. Functionally classified (KOs)
803 metatranscriptomic reads; 2/4 components, g. Functionally classified (KOs) metaproteomic
804 spectra; 2/4 components. The numbers in taxon names (b, c) are identifiers from the mOTUs
805 workflow. For KOs (e-g), details are provided in Supplementary Table 3.

806 **Extended Data Figure 3. Microbial diversity and differential abundance comparisons of**
807 **taxonomic and functional data.** a. Alpha diversity and group in taxonomically classified
808 metagenomic (MG) and metatranscriptomic (MT) sequence reads; box hinges: 1st and 3rd
809 quartiles; whiskers: hinge to highest/lowest values that is within 1.5*IQR of hinge; gray cross:
810 mean, b. Beta diversity and group (Non-metric Multidimensional Scaling based on Bray-Curtis
811 dissimilarity) in MG and MT species data, with ellipses showing 95% confidence, c. Number of
812 differentially abundant taxa (q (false discovery rate adjusted P) < 0.05); MG and MT data tested
813 with DESeq2 and MP with ANOVA (age and sex adjusted) and two-sided t-tests, d. Genera with
814 $q < 0.05$ in MG or MT data for the two-group case (either PD or iRBD) vs control contrast, e.
815 Number of differentially abundant ($q < 0.05$) KEGG orthologs (KOs) in MG, MT, and
816 metaproteomic (MP) data;); MG and MT data tested with DESeq2 and MP with ANOVA (age
817 and sex adjusted) and two-sided t-tests, e. 10 pathways most commonly represented by the
818 differentially abundant KOs ($q < 0.05$) for the case vs control comparison in MG, MT and MP
819 data. In heatmaps, . $0.1 > q > 0.05$, * $q < 0.05$, ** $q < 0.01$, *** $q < 0.001$.
820 **Extended Data Figure 4. Additional results for metabolomics**. a. Metabolites with q (false
821 discovery rate adjusted P) < 0.05 for the two-group case (PD or iRBD) vs control contrast and at
822 least one pair of three-category groups, b. 2-HP normalized peak area and disease duration in PD
823 patients; grey values = full data, black values = two longest-duration subjects excluded, c. 2-HP in
824 plasma (targeted metabolomics); 2 extreme outliers excluded (2-HP concentration > 30 μM, both
825 in the iRBD group); box hinges: 1st and 3rd quartiles; whiskers: hinge to highest/lowest values
826 that is within 1.5*IQR of hinge; grey cross: mean, d. Correlations of metabolites and taxa,
827 showing taxa with $q < 0.05$ in more than 20 comparisons out of a total of 32 approaches: 2
828 metabolites, 2 data types (MG or MT), 2 annotation methods (Kraken or mOTUs), 2

829 normalizations (RA = relative abundance, CLR = centered log ratio transform) and 2 correlation
830 coefficients (Pearson or Spearman), e. Correlations of 2-HP and β-glutamate and other metabolites,
831 showing top 5 by q in full data for each metabolite and correlation coefficient, f. 10 most common
832 pathways represented by KEGG orthologs significantly correlated with 2-HP ($q < 0.05$, and for
833 MG and MT data, absolute value of correlation coefficient > 0.4). In all plots, MG = metagenomic
834 data, MT = metatranscriptomic data, MP = metaproteomic data. In plots with stars, . $0.1 > q >$
835 0.05, * $q < 0.05$, ** $q < 0.01$, *** $q < 0.001$.

836 **Extended Data Figure 5. Results of integrated multi-omics with DIABLO.** The classification
837 was run for the two-category case (iRBD or PD) vs control variable, selecting the 5 best features
838 for differentiating between these categories on 2 axes for each of the seven data types (MG =
839 metagenomic, MT = metatranscriptomic, MP = metaproteomic; KOs: functional annotations as
840 represented by KEGG orthologs). a. Design matrix used for DIABLO, calculated based on running
841 PLS for each pair of data blocks, b. Component tuning, based on which 2 was selected as the
842 number of components to use; ER = error rate, BER = balanced error rate, error bars = standard
843 deviations, c. Plots of samples and sample classes per data type; green triangles with dashed lines
844 = controls, black circles with soldi lines = PD and iRBD patients, ellipses represent 95%
845 confidence d. Correlation circle plot showing the selected features together, with labels for MG
846 and MT taxa and metabolites, e. Loadings for the five selected features for each data type and
847 component. Annotations for the selected KOs are provided in Supplementary Table 10.

848 **Extended Data Figure 6. Additional results on 2-hydroxypyridine and genus**
849 ***Methanobrevibacter*.** a. log10(relative abundance) of metagenomic reads classified as
850 *Methanobrevibacter smithii* by diagnosis group in main study cohort, b. log10(relative abundance)
851 of metatranscriptomic reads classified as *Methanobrevibacter smithii* by diagnosis group in main

852 study cohort, c. % of metaproteomic spectra classified as *Methanobrevibacter* by diagnosis group
853 in the main study cohort, d. log10(relative abundance) of 16S rRNA gene amplicons classified as
854 *Methanobrevibacter* in the Luxembourgish NCER- PD cohort. e. Summaries of *q*-values (fdr-
855 adjusted *P*-values) of correlations for 2-hydroxypyridine and 74 methanogenesis-related genes
856 found in the sequence data (tested either in full data or with data containing samples of a specific
857 group, as given on the x-axis). f. % of samples with predicted proteins containing the HmdB or
858 HmdC genes, which code for the biosynthesis of the cofactor for Hmd. g 2-hydroxypyridine
859 normalized peak area depending on the presence of HmdB or HmdC gene in samples. MG =
860 metagenomic data, MT = metatranscriptomic data; in boxplots, box hinges: 1st and 3rd quartiles;
861 whiskers: hinge to highest/lowest values that is within 1.5*IQR of hinge; grey cross: mean.

862 **Extended Data Figure 7. Additional results from the HiTox yeast model.** a. Representative
863 growth curves of control and HiTox strains in presence of 2-hydroxypyridine (2-HP) at the
864 indicated concentrations. b. 2-HP dose-response assay in uninduced condition in HiTox and
865 control strains. c. Dose-response assay in control strain and HiTox strain in aSyn-expressing
866 condition after treatment with either 2-HP, 3-hydroxypyridine (3-HP) or 4- hydroxypyridine (4-
867 HP). In b and c, OD_{600} was measured 48 h after inoculation and mean and SD were calculated
868 from four biological replicates.

869 **Extended Data Figure 8. Additional results from the induced human pluripotent stem cell**
870 **enteric neuron model.** a. Induced human pluripotent stem cell characterization stainings show
871 robust expression of OCT4, SEEA4 and NANOG pluripotency markers. Scale bars: 200 µm. b.
872 Enteric neuron characterisation stainings at 40 days of differentiation detect presence of neural
873 crest stem cell markers MASH1 and PHOX2A, and of different neuronal identities, such as
874 GABAergic, serotoninergic and dopaminergic. Scale bars: 100 µm. c. Relative viability after 2-

875 hydroxypyridine exposure. Comparison to untreated sample was not significant when evaluated
876 with a Kruskal-Wallis test. d. High-content imaging of apoptosis marker cleaved-caspase 3 (CC3),
877 TUJ1-positive neurons and Hoechst-positive nuclei. Nuclei images contain a representation of the
878 mask applied to segment the nuclei; scale bar: 100 μm. e. Quantification of CC3-positive staining
879 normalized to the amount of TUJ1-positive neurons. In c and d, data is represented as mean ± SEM
880 of three independent neuronal differentiations, with 30 fields per well and 8 wells per condition
881 quantified for each. ** $P < 0.01$.

882 **Extended Data Figure 9. Effects of intrastriatal injections of 100 mM 2-hydroxypyridine in**
883 **transgenic mouse model of PD on phospho-aSyn accumulation in different brain regions.** a.
884 Striatum: 2-HP-induced decrease of phospho-aSyn signals in synaptic boutons; scale bar: 50 μm,
885 b. Substantia nigra: 2-HP-induced non-significant increase of phospho-aSyn in synaptic boutons;
886 scale bar: 350 μm, c. Prefrontal cortex: 2-HP-induced significant increase of phospho-aSyn signals
887 in cell body profiles with neuronal morphology (double-stained with DAPI, lower row of images);
888 scale bar: 50 μm. Microphotographs show examples for 0 mM and 100 mM in hSNCA mice only.
889 Bar plots show mean and standard deviation; n of mice = 5-8 per group. *P*-values are given between
890 group means that are different. * $P < 0.05$.

891

Supplementary Files

This is a list of supplementary files associated with this preprint. Click to download.

- supplementaryinformation.pdf
- extendeddata.pdf
- supplementarytables.xlsx